Provided for non-commercial research and education use.
Not for reproduction, distribution or commercial use.

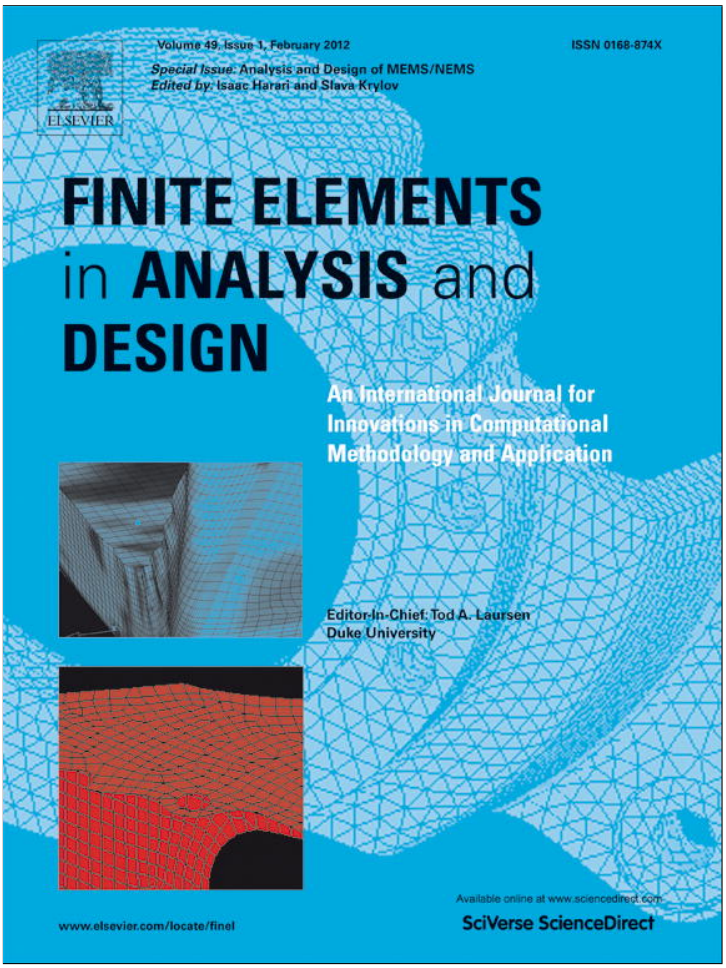

This article appeared in a journal published by Elsevier. The attached copy is furnished to the author for internal non-commercial research and education use, including for instruction at the authors institution and sharing with colleagues.

Other uses, including reproduction and distribution, or selling or licensing copies, or posting to personal, institutional or third party websites are prohibited.

In most cases authors are permitted to post their version of the article (e.g. in Word or Tex form) to their personal website or institutional repository. Authors requiring further information regarding Elsevier's archiving and manuscript policies are encouraged to visit:

http://www.elsevier.com/copyright

Author's personal copy

Finite Elements in Analysis and Design 49 (2012) 3–12

Contents lists available at SciVerse ScienceDirect

Finite Elements in Analysis and Design

journal homepage: www.elsevier.com/locate/finel

Bridging the gap between experimental measurements and atomistic predictions of the elastic properties of silicon nanowires using multiscale modeling

Geng Yun [a], Harold S. Park [b,*]

[a] Department of Mechanical Engineering, University of Colorado, Boulder, CO 80309, United States
[b] Department of Mechanical Engineering, Boston University, Boston, MA 02215, United States

ARTICLE INFO

Article history:
Received 24 October 2010
Received in revised form
22 April 2011
Accepted 12 June 2011
Available online 13 September 2011

Keywords:
Surface Cauchy–Born
Silicon
Nanowire
Finite elements
Surface stress
Bending

ABSTRACT

In the present work, we have applied recently developed nonlinear multiscale finite element techniques which account for nanoscale surface stress and surface elastic effects to investigate the elastic properties of silicon nanowires as obtained through bending deformation. The numerical results are used to clarify the factors underlying the current disconnect between atomistic simulations and experiments as to the nanowire sizes at which deviation from bulk elastic properties due to surface effects are observed. In particular, we demonstrate that when nanowires with aspect ratios (defined as the axial length divided by the square cross sectional length) larger than about 15 are considered, the elastic softening that has been observed experimentally for larger (i.e. >20 nm diameter) nanowires is observed. In contrast, when smaller aspect ratios are considered, very little deviation from the bulk elastic properties are observed, in agreement with existing atomistic calculations. Furthermore, we demonstrate that the elastic softening is strongly boundary condition dependent, where fixed/fixed silicon nanowires exhibit a strong aspect ratio-dependent softening, while little variation in the elastic properties of fixed/free nanowires are observed. Comparisons are made with existing surface elastic theories and experiments to bring further insights into the boundary condition dependence in elastic properties.

© 2011 Elsevier B.V. All rights reserved.

1. Introduction

Semiconducting nanowires have been intensely researched by both the scientific and engineering communities over the past decade [1,2]. One of the major reasons for the surge in interest for nanowires has been due to their potential as the basic building block for nanoelectromechanical systems (NEMS) [3]. Of semiconducting nanowires, silicon is one of the most important, due to its optoelectronic properties [4], piezoresistivity [5], thermoelectric potential [6,7], and other unique physical properties [1,3,8,9].

Due to the fact that nanowires have beam-like geometries and because many of the potential NEMS applications require knowledge of the nanowire elastic properties, there has been a recent surge of interest in both experimental and theoretical techniques to characterize the elastic properties of silicon nanowires. Silicon nanowires are expected to have elastic properties, such as Young's modulus, that deviate from the bulk value due to nanoscale surface stress [10] and surface elastic effects [11], both of which arise due to the coordination number reduction [12] that characterizes surface atoms as compared to those that lie within the material bulk. The coordination number reduction implies that surface atoms have a different stiffness than do bulk atoms, since the stiffness is related to the number of bonding neighbors an atom has. Furthermore, because surface atoms are not at equilibrium unlike atoms in the bulk, the coordination number reduction leads to a surface stress, which has an increasingly important effect on the mechanical behavior and properties of nanowires with decreasing size, as demonstrated in many previous works [13–16]. Furthermore, this difference in stiffness between surface and bulk atoms has an increasingly large effect on the overall elastic properties of the nanowires with decreasing nanowire size, or increasing surface area to volume ratio.

The elastic properties of silicon nanowires have been studied experimentally using a variety of techniques, including resonance [17], bending [18–23], and tension [24–26]. While these experiments have considered the silicon nanowires with diameters ranging from about 20–200 nm, and with different axial ($\langle 110\rangle$, $\langle 111\rangle$) and surface orientations, most have reported a decrease in Young's modulus with decreasing diameter [9], with the elastic softening being most strikingly observed in recent

* Corresponding author.
E-mail address: parkhs@bu.edu (H.S. Park).

0168-874X/$ - see front matter © 2011 Elsevier B.V. All rights reserved.
doi:10.1016/j.finel.2011.08.014

Author's personal copy

tension [24–26], resonance [17] and bending [22] investigations, particularly when the nanowire diameter decreases below about 100 nm [9]. We note in contrast that others have reported no change in elastic modulus with decreasing size [18].

Theoretically, atomistic simulations based upon classical molecular dynamics (MD) or density functional theory (DFT) have been utilized to determine the elastic properties of silicon nanowires [11,27–31]. Similar to the experimental results, a significant softening in the Young's modulus of the silicon nanowires has been reported in all MD investigations. However, the MD simulations [11,29] and density functional studies [28,31] show a large disparity as compared to the experimental results in that they both predict that the Young's modulus of the silicon nanowires reaches the bulk value for nanowire diameters larger than about 5–10 nm.

The preceding discussion makes clear that there exists a substantial gap between computational predictions and experimental measurements of the Young's modulus of semiconducting nanowires. In particular, while experimental measurements of the silicon nanowire Young's modulus deviates from the bulk Young's modulus at diameters smaller than about 100 nm, similar deviations from the bulk Young's modulus are not observed for wire diameters larger than approximately 10 nm [9].

Therefore, it is the objective of the present work to shed insights into the factors causing this gap between experimental and computational predictions of the Young's modulus of silicon nanowires. To do so, we utilize the recently developed surface Cauchy–Born (SCB) model [32–34], which is a multiscale, nonlinear finite element (FE)-based computational model that captures surface stress and surface elastic effects on the mechanical behavior and properties of nanomaterials, to study the elastic properties of $\langle 100 \rangle$ silicon nanowires with unreconstructed {100} transverse surfaces as obtained through bending simulations. In order to bridge the length scale gap between the nanowire diameters that are studied experimentally and computationally, we study silicon nanowires that have cross sectional dimensions ranging from 12 to 30 nm.

The simulations demonstrate that there are two important considerations that can explain the disconnect between MD simulations and experiment. First, we show that the elastic softening that is exhibited by the nanowires is strongly aspect ratio dependent. In particular, an increase in the nanowire aspect ratio is shown to significantly reduce the elastic stiffness of the nanowires in agreement with existing experimental data [22,25,26], where nanowires with cross sectional sizes of 30 nm are shown to be significantly softer than the corresponding bulk material. Second, we demonstrate that the elastic softening is strongly boundary condition-dependent, as fixed/fixed nanowires are significantly softer elastically than are fixed/free nanowires. Both results are justified through comparisons with existing surface elastic solutions for the effective modulus of silicon nanowires [35].

2. Bulk and surface Cauchy–Born models for silicon

The SCB model is an extension of the standard bulk Cauchy–Born (BCB) model, which is a multiscale, nonlinear, finite deformation constitutive relationship that enables the calculation of continuum stress and stiffness directly from an underlying interatomic potential energy. The BCB model has previously been utilized by various authors to study the mechanical behavior and properties of both metals [36], semiconductors [37–39], and carbon-based nanostructures [40,41]. One key shortcoming of the classical BCB model is that it does not admit surface effects, since all material points are assumed to be part of an infinite, periodic crystal.

Because of this, Park et al. have recently developed the SCB model [32–34], which extends the BCB model such that the system total energy includes contributions from not only the bulk, but also the surface atoms. In doing so, they were able to develop multiscale, FE-based computational models that enabled the three-dimensional solution of nanomechanical boundary value problems while accounting for nanoscale surface stress and surface elastic effects within a nonlinear, finite deformation framework.

The SCB model was previously developed for both face-centered-cubic (FCC) metals [32,33] and non-centrosymmetric diamond cubic lattices such as silicon [34], and applied to nanomechanics and NEMS-related problems ranging from nanoscale resonant mass sensing [42], thermomechanical coupling [43], resonant frequencies, and elucidating the importance of nonlinear, finite deformation kinematics on the resonant frequencies of both FCC metal [44] and silicon nanowires [45,46], strain sensing [47], bending of FCC metal nanowires [48], length/time scale bridging for dynamic multiscale simulations [49], and electromechanical coupling in surface-dominated nanostructures [50].

Because the details regarding the SCB model for silicon, its differences from the standard BCB model, and its FE implementation have been described in previous publications [34,45], we give an abbreviated explanation for the SCB model for silicon in the present work.

2.1. Bulk Cauchy–Born model

In the present work, we utilize the T3 form of the Tersoff potential [51] and the resulting parameters to describe both the bulk and surface elastic properties of silicon. The T3 is named as such due to the fact that two earlier versions of the Tersoff potential suffered from various shortcomings, including not predicting diamond as the ground state of silicon, inaccuracies in the bulk elastic constants [52], and inaccurate modeling of the {100} surfaces of silicon [10]. The T3 form of the Tersoff potential can be written as

$$U = \frac{1}{2}\sum_{i \neq j} V_{ij},$$

$$V_{ij} = f_C(r_{ij})(f_R(r_{ij}) + b_{ij} f_A(r_{ij})), \tag{1}$$

where r_{ij} is the distance between atoms i and j, f_C is a cut-off function, which is used to ensure that the Tersoff potential is effectively a nearest neighbor potential, f_R is a repulsive function, f_A is an attractive function, and b_{ij} is the bond order function, which is used to modify the bond strength depending on the surrounding environment. The various functions all have analytic forms, which are given as

$$f_R(r_{ij}) = A \exp(-\lambda r_{ij}), \tag{2}$$

$$f_A(r_{ij}) = -B \exp(-\mu r_{ij}), \tag{3}$$

$$b_{ij} = (1 + \beta^n \zeta_{ij}^n)^{-1/2n}, \tag{4}$$

where

$$\zeta_{ij} = \sum_{k \neq i,j} f_C(r_{ik}) g(\theta_{ijk}) \tag{5}$$

and

$$g(\theta_{ijk}) = 1 + \frac{c^2}{d^2} - \frac{c^2}{d^2 + (h - \cos\theta_{ijk})^2}. \tag{6}$$

Aside from θ_{ijk}, which represents the angle between a triplet of atoms i, j and k, the remaining constants in (2)–(6) are all parameters of the Tersoff potential, whose values are given in Table 1.

Author's personal copy

Table 1
Tersoff T3 potential parameters [51].

Parameter	Value
A	1830.8 eV
B	471.18 eV
λ	2.4799 Å^{-1}
μ	1.7322 Å^{-1}
β	1.1×10^{-6}
c	100,390
d	16.217
h	−0.59825
n	0.78734
R_C	2.70 Å

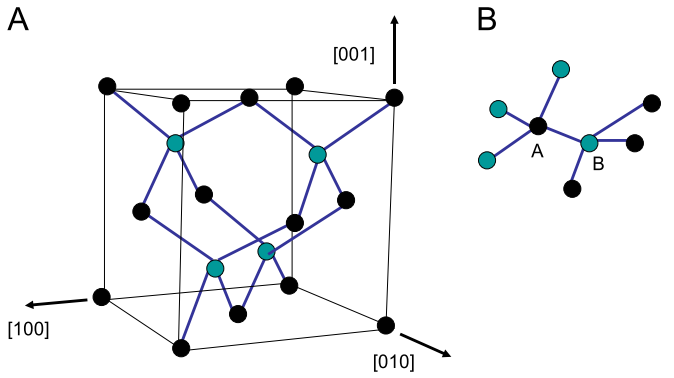

Fig. 1. Illustration of the diamond cubic lattice structure of silicon. Black atoms represent standard FCC unit cell atoms, while green atoms represent the interpenetrating FCC lattice. The drawn bonds connect atoms in FCC lattice B to atoms in FCC lattice A. (For interpretation of the references to color in this figure legend, the reader is referred to the web version of this article.)

The bond order function (4) is the part of the potential that incorporates many-body effects through the θ_{ijk} term in Eqs. (5) and (6). Thus, for each bond i-j, the bond order term b_{ij} depends on the number of neighboring atoms j-k that fall within a certain cutoff radius $f_C(r_{ik})$ from atom i.

The Tersoff potential was designed as a nearest neighbor potential, due to the computational expense involved in evaluating the bond order function b_{ij} for many atomic pairs. For a bulk atom, this implies that it will have exactly four nearest neighbors in the undeformed or initial configuration. Thus, the energetics of a representative bulk atom in a silicon diamond cubic (DC) lattice can be reproduced using a five-atom unit cell, following that as introduced by Tang et al. [38], where the center atom A in Fig. 1(B) represents the first FCC bravais lattice, and the surrounding four atoms B represent the atoms on the second FCC bravais lattice.

The fact that the DC lattice is composed of two interpenetrating FCC lattices has important implications for formulating a BCB model. The first is that the DC lattice structure is not centrosymmetric, which means that the unit cell must contain more than a single atom, and leads to additional computational expense in modeling the larger unit cell. The second important fact is that the two interpenetrating FCC lattices must be able to translate rigidly with respect to each other, necessitating the introduction of an internal degree of freedom $\boldsymbol{\Xi}$ for each unit cell. The internal degree of freedom $\boldsymbol{\Xi}$ is associated with atom A in Fig. 1(B), indicating that it can translate rigidly with respect to the B atoms in the second bravais lattice. This internal degree of freedom $\boldsymbol{\Xi}$ serves an identical purpose as the shift vector that has been introduced in the BCB modeling of carbon nanotubes [40,41].

Converting the T3 potential energy (1) into a strain energy density Φ to account for a five atom bulk unit cell, we write, following Tang et al. [38]

$$\Phi = \frac{1}{2\Omega_0}\sum_{j=2}^{5} V_{1j}(r_{1j}), \tag{7}$$

where $i=1$ in (7) because atom i is considered the center of the unit cell, and the summation goes over the four nearest neighbor bonds $j=2,3,4,5$. The full expression for the strain energy density Φ can be written as

$$\Phi = \frac{1}{2\Omega_0}\sum_{j=2}^{5} V_{1j} = \frac{1}{2\Omega_0}\sum_{j=2}^{5} f_c(r_{1j}) \times\left(A\exp(-\lambda r_{1j}) - B\exp(-\mu r_{1j})\left(1+\beta^n\left(\sum_{k\neq 1,j} f_c(r_{1k})g(\theta_{1jk})\right)^n\right)^{-1/2n}\right), \tag{8}$$

where again the multibody effects of the bonding environment are captured through the $g(\theta_{1jk})$ term. The strain energy density in (8) can be turned into an object that is useful for BCB modeling by making the bond lengths r_{1j} functions of the continuum deformation quantities and the internal degree of freedom as

$$r_{1j} = |\mathbf{r}_{1j}| = |\mathbf{F}(\mathbf{R}_{1j}+\boldsymbol{\Xi})|, j = 2,3,4,5 \tag{9}$$

where $\mathbf{r}_{1j}$ is the deformed bond vector, $\mathbf{R}_{1j}$ is the undeformed bond vector between atoms 1 and j, $\boldsymbol{\Xi}$ is the shift degree of freedom that is necessary to capture rigid body translation between the two interpenetrating FCC lattices that comprise a silicon (diamond cubic) lattice, $\mathbf{F}$ is the deformation gradient from nonlinear continuum mechanics, and $\mathbf{C}=\mathbf{F}^T\mathbf{F}$ is the right Cauchy–Green stretch tensor. The incorporation of the internal degrees of freedom and writing the bond lengths in terms of $\mathbf{F}$ results in a modified strain energy density function as

$$\Phi(\mathbf{C}) = \tilde{\Phi}(\mathbf{C},\boldsymbol{\Xi}(\mathbf{C})). \tag{10}$$

We can calculate the second Piola–Kirchoff (PK2) stress $\mathbf{S}$ as

$$\frac{1}{2}\mathbf{S} = \frac{\partial\Phi}{\partial\mathbf{C}} = \frac{\partial\tilde{\Phi}}{\partial\mathbf{C}} + \frac{\partial\tilde{\Phi}}{\partial\boldsymbol{\Xi}}\frac{\partial\boldsymbol{\Xi}}{\partial\mathbf{C}}. \tag{11}$$

To keep the crystal at an energy minimum, the internal degrees of freedom are constrained to deform according to $\boldsymbol{\Xi}^*$, which leads to the following relationship:

$$\frac{\partial\tilde{\Phi}}{\partial\boldsymbol{\Xi}^*} = 0, \tag{12}$$

which reduces the expression for the PK2 stress in (11) to

$$\mathbf{S} = 2\frac{\partial\tilde{\Phi}}{\partial\mathbf{C}}. \tag{13}$$

We calculate the tangent modulus as

$$\frac{1}{4}\mathcal{C}_{IJKL} = \frac{\partial^2\Phi}{\partial\mathcal{C}_{KL}\partial\mathcal{C}_{IJ}} = \frac{\partial^2\tilde{\Phi}}{\partial\mathcal{C}_{KL}\partial\mathcal{C}_{IJ}} + \frac{\partial^2\tilde{\Phi}}{\partial\Xi_q\partial\mathcal{C}_{IJ}}\frac{\partial\Xi_q}{\partial\mathcal{C}_{KL}} + \frac{\partial\tilde{\Phi}}{\partial\Xi_p}\frac{\partial^2\Xi_p}{\partial\mathcal{C}_{KL}\partial\mathcal{C}_{IJ}} + \left(\frac{\partial^2\tilde{\Phi}}{\partial\mathcal{C}_{KL}\partial\Xi_p} + \frac{\partial^2\tilde{\Phi}}{\partial\Xi_q\partial\Xi_p}\frac{\partial\Xi_q}{\partial\mathcal{C}_{KL}}\right)\frac{\partial\Xi_p}{\partial\mathcal{C}_{IJ}}. \tag{14}$$

(14) can be simplified by the knowledge that $\partial\boldsymbol{\Xi}/\partial\mathbf{C}$ needs to be evaluated for the equilibrium preserving motion $\boldsymbol{\Xi}^*$, which leads to the expression

$$\frac{\partial^2\tilde{\Phi}}{\partial\mathcal{C}_{KL}\partial\Xi_p^*} + \frac{\partial^2\tilde{\Phi}}{\partial\Xi_q^*\partial\Xi_p^*}\frac{\partial\Xi_q^*}{\partial\mathcal{C}_{KL}} = 0. \tag{15}$$

Solving (15) gives

$$\frac{\partial\Xi_q^*}{\partial\mathcal{C}_{KL}} = -\left(\frac{\partial^2\tilde{\Phi}}{\partial\Xi_q^*\partial\Xi_p^*}\right)^{-1}\frac{\partial^2\tilde{\Phi}}{\partial\mathcal{C}_{KL}\partial\Xi_p^*}. \tag{16}$$

Author's personal copy

Using (16), the spatial tangent modulus can be expressed as

$$\mathcal{C}_{IJKL} = M_{IJKL} - A_{IJp}A_{KLq}(\mathbf{D}^{-1})_{pq}, \tag{17}$$

where

$$M_{IJKL} = 4\frac{\partial^2 \tilde{\Phi}}{\partial \mathcal{C}_{IJ}\partial \mathcal{C}_{KL}},$$
$$D_{pq} = \frac{\partial^2 \tilde{\Phi}}{\partial \Xi^*_p \partial \Xi^*_q},$$
$$A_{IJp} = 2\frac{\partial^2 \tilde{\Phi}}{\partial \mathcal{C}_{IJ}\partial \Xi^*_p}. \tag{18}$$

2.2. Surface Cauchy–Born model

For the SCB model, we consider a nine-atom surface unit cell, as previously described by Park and Klein [34], and as illustrated in Fig. 2. The resulting strain energy density γ for the nine-atom surface unit cell can thus be written as

$$\gamma = \frac{1}{\Gamma_0}\left(\sum_{j=2,6} V_{1j}(r_{1j}) + \sum_{k=1,7,8,9} V_{6k}(r_{6k}) + \sum_{m=1,3,4,5} V_{2m}(r_{2m})\right), \tag{19}$$

where Γ_0 is the area per atom on the surface. Following (9), we express the bond lengths for the surface unit cell as

$$r_{1j} = |\mathbf{r}_{1j}| = |\mathbf{F}(\mathbf{R}_{1j} + \Xi^s)|, \quad j = 2,6,$$
$$r_{6k} = |\mathbf{r}_{6k}| = |\mathbf{F}(\mathbf{R}_{6k} + \Xi^s)|, \quad k = 1,7,8,9,$$
$$r_{2m} = |\mathbf{r}_{2m}| = |\mathbf{F}(\mathbf{R}_{2m} + \Xi^s)|, \quad m = 1,3,4,5. \tag{20}$$

Incorporating the bond lengths that have been modified by the deformation gradient $\mathbf{F}$ and the internal surface degrees of freedom Ξ^s in (20) creates a modified surface energy density $\tilde{\gamma}(\mathbf{C})$ from (19), where the surface energy density has been modified analogous to the procedure outlined previously for the bulk energy density in (11) and (12) to enforce the energy minimizing condition

$$\frac{\partial \tilde{\gamma}}{\partial \tilde{\Xi}^s} = 0, \tag{21}$$

where $\tilde{\Xi}^s$, similar to the meaning in the bulk case in (12), represents the deformation of the surface internal degrees of freedom necessary to minimize the surface energy. Using the modified surface energy density $\tilde{\gamma}(\mathbf{C})$, we arrive at the expression

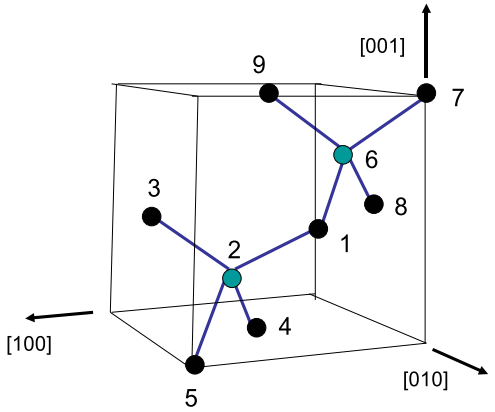

Fig. 2. Illustration of the nine atom surface unit cell for the surface with a [010] normal of a diamond cubic crystal. Black atoms represent FCC lattice A, while green atoms represent the interpenetrating FCC lattice B. The drawn bonds connect atoms in FCC lattice B to atoms in FCC lattice A. (For interpretation of the references to color in this figure legend, the reader is referred to the web version of this article.)

for the surface PK2 stress $\mathbf{S}^s(\mathbf{C})$, where the superscript s here and below indicates surface values

$$\mathbf{S}^s(\mathbf{C}) = 2\frac{\partial \tilde{\gamma}(\mathbf{C})}{\partial \mathbf{C}}. \tag{22}$$

We call the stress in (22) a surface stress because it is not a stress in the traditional sense, i.e. the normalization factor is an area, instead of a volume. Therefore, the units of the surface stress are force/length, as opposed to the force/area units typically found for bulk stresses. In addition, the surface stresses $\mathbf{S}^s(\mathbf{C})$ are 3×3 tensors with normal components which allow surface relaxation due to undercoordinated atoms lying at material surfaces [32,33]; discussion of these points and a detailed comparison of the SCB model to the classical Gurtin–Murdoch theory of surface elasticity [53] will be given in a later section.

Similarly, the surface tangent modulus can be written as

$$\mathcal{C}^s_{IJKL} = M^s_{IJKL} - A^s_{IJp}A^s_{KLq}(\mathbf{D}^{-1})^s_{pq}, \tag{23}$$

where

$$M^s_{IJKL} = 4\frac{\partial^2 \tilde{\gamma}}{\partial \mathcal{C}^s_{IJ}\partial \mathcal{C}^s_{KL}},$$
$$D^s_{pq} = \frac{\partial^2 \tilde{\gamma}}{\partial \tilde{\Xi}^s_p \partial \tilde{\Xi}^s_q},$$
$$A^s_{IJp} = 2\frac{\partial^2 \tilde{\gamma}}{\partial \mathcal{C}^s_{IJ}\partial \tilde{\Xi}^s_p}. \tag{24}$$

2.3. Governing equilibrium finite element equations

Having defined both the bulk and surface energy densities $\tilde{\Phi}(\mathbf{C})$ and $\tilde{\gamma}(\mathbf{C})$ for the bulk and surface unit cells, we can immediately write the total potential energy Π of the system by combining the bulk and surface energies while including the work done by external loads $\mathbf{T}$ as

$$\Pi(\mathbf{u}) = \int_{\Omega_0^{bulk}} \tilde{\Phi}(\mathbf{C})\, d\Omega + \int_{\Gamma_0} \tilde{\gamma}(\mathbf{C})\, d\Gamma - \int_{\Gamma_0} (\mathbf{T}\cdot\mathbf{u})\, d\Gamma. \tag{25}$$

In order to obtain a form suitable for FE calculations, we introduce the standard discretization of the displacement field $\mathbf{u}(\mathbf{X})$ using FE shape functions as

$$\mathbf{u}(\mathbf{X}) = \sum_{I=1}^{nn} N_I(\mathbf{X})\mathbf{u}_I, \tag{26}$$

where N_I are the shape or interpolation functions, nn are the total number of nodes in the discretized continuum, and $\mathbf{u}_I$ are the displacements of node I [54,55]. Substituting (19), (7) and (26) into (25) and differentiating gives the minimizer of the potential energy and also the FE nodal force balance [54]:

$$\frac{\partial \Pi}{\partial \mathbf{u}_I} = \int_{\Omega_0^{bulk}} \mathbf{B}^T\mathbf{S}\mathbf{F}^T\, d\Omega + \int_{\Gamma_0} \mathbf{B}^T\mathbf{S}^s\mathbf{F}^T\, d\Gamma - \int_{\Gamma_0} N_I\mathbf{T}\, d\Gamma, \tag{27}$$

where $\mathbf{S}$ is the PK2 stress due to the bulk strain energy, $\mathbf{S}^s$ is the surface PK2 stress defined in (22), $\mathbf{B}^T$ represents the derivative of the strain with respect to $\mathbf{u}_I$, and where the displacements $\mathbf{u}$ can be related to the right stretch tensor $\mathbf{C}$ by first noting that the deformation gradient $\mathbf{F} = 1 + d\mathbf{u}/d\mathbf{X}$, and then taking the definition of the right stretch tensor $\mathbf{C} = \mathbf{F}^T\mathbf{F}$.

What has been accomplished in (27) is a systematic manner of obtaining continuum stress measures by calculating the system potential energy as a function of bulk and surface components. By correctly calculating the system energy, standard continuum mechanics relationships can be utilized to derive stress measures

Author's personal copy

for usage in FE computations. The salient feature of Eq. (27) is that as the surface area to volume ratio becomes larger, the surface area terms will dominate the energetic expression. Because the stresses required for the FE internal forces are calculated by differentiating the strain energy density, correctly accounting for the surface energy will naturally lead to the correct forces on surface nodes. In contrast, if the volume of the bulk material is significantly larger than the surface area, then the potential energy from the surface terms will be insignificant compared to the volumetric potential energy, and the material will feel no effect from the surface stresses. Thus, this model degenerates to a BCB model as the length scale of the material increases.

2.3.1. Comparison to classical surface elasticity-based computational models

It is worth noting that the approach and philosophy taken in developing the SCB model is different from that taken by other authors in capturing nanoscale surface effects on the mechanical behavior and properties of nanomaterials within a computational, FE-based framework. Most of these computational models [56–60] are based upon a FE discretization of the governing surface elasticity equations of Gurtin and Murdoch [53], where the surface stress is written as, in the traditional thermodynamic definition [61,62]

$$\tau = \tau_0 + \mathbf{C_0}\varepsilon, \tag{28}$$

where τ is the surface stress, τ_0 is the residual (strain-independent) portion of the surface stress, and $\mathbf{C_0}\varepsilon$ is the surface-elastic (strain-dependent) part of the surface stress, where $\mathbf{C}_0$ is the (constant) surface elastic stiffness. We note that the definition of surface stress in (28) is based upon linear elastic, small deformation kinematics; a review of surface elastic formulations within the Gurtin–Murdoch context was recently performed by Wang et al. [63].

The thermodynamic interpretation of the surface stress τ in (28) is that of an excess quantity, i.e. a measure of the difference as compared to the equivalent bulk quantity. The SCB surface energy density $\gamma(\mathbf{C})$ in (19) differs from the conventional thermodynamic definition of surface energy density in that it does not represent the excess, or difference in energy density as compared to a typical bulk atom; instead, it represents the actual potential energy density of an atom lying at the surface of a nanostructure.

However, the definition of surface energy density utilized in the present work in (19) is extremely favorable for nonlinear FE calculations. In particular, in an actual MD simulation, the force on a given atom, whether it lies within the bulk or on the surface, is obtained by differentiating its actual potential energy, and not its excess energy, i.e. the difference of potential energy as compared to an ideal bulk atom. Therefore, the SCB definition of surface energy density in (19) leads directly to a surface stress, and thus an internal surface force in (27) that is similar in meaning to the force obtained on a surface atom in an MD calculation.

Another important point of distinction is that the surface stress τ that results from the classical thermodynamic definition in (28) is a 2×2 in-plane tensor. We note the recent work of Javili and Steinmann [64,65], who also discretized a total energy similar to (27) in the present work; however, the resulting surface stress in that work was also a 2×2 in-plane tensor. In other words, the component of the stress normal to the surface is zero. The implication of this 2×2 in-plane surface stress tensor is that, within the Gurtin–Murdoch formulation, the surface is assumed to be formed at equilibrium. This assumption contains drawbacks for many of the important surface-related physics and properties that are observed in nanomaterials.

For example, surface stresses are known to cause extreme lattice contractions leading to unexpected shape memory and pseudoelastic behavior in certain FCC metal nanowires that are not observed in the corresponding bulk material [13–15]; surface stresses can also cause sufficient compressive deformation in FCC metal nanowires to induce nonlinear elastic stiffening and softening [66], while surface stresses cause FCC metals and silicon nanostructures to exhibit different types of surface relaxations [10]. Due to the 2×2 in-plane nature of the surface stress tensor that emerges from Gurtin–Murdoch surface elasticity, it is unclear whether such surface-stress-driven relaxation effects can be captured within that framework.

In contrast, the surface stress that emerges from the SCB model is 3×3 and includes the out of plane stress component. This emerges naturally due to the fact that the deformation gradient, or stretch tensor that is utilized in the SCB formulation at the surface is also fully 3D. This is rationalized by the fact that surface atoms should have an out of plane degree of freedom such that they can relax normal to the free surface. Importantly, the SCB model has been shown to accurately capture the surface-stress-driven relaxation in comparison to direct atomistic simulations for both FCC metal [33] and semiconducting/silicon nanowires [34,45].

The SCB model has recently been utilized to demonstrate the importance of finite deformation kinematics (in contrast to the linear surface elasticity model shown in (28)) and to illustrate the effect of the residual surface stress on the resonant frequencies of both FCC metal and silicon nanowires if finite deformation kinematics are considered [44,46]. The key finding was that if finite deformation kinematics are considered, the strain-independent surface stress τ_0 substantially alters the resonant frequencies of the nanowires; however, the strain-dependent surface stress $\mathbf{C}_0\varepsilon$ has a significant effect, one that can be comparable to or even larger than the effect of the strain-independent surface stress depending on the boundary condition, in shifting the resonant frequencies of the nanowires as compared to the bulk material.

In addition to the arguments presented above for the need for finite deformation kinematics with regard to surface stress effects on the resonant frequencies, the importance of finite deformation kinematics also emerges due to the surface-stress-driven relaxation phenomena discussed above. Specifically, because the Gurtin–Murdoch theory is based upon linear elasticity for not only the surface but also for the bulk, important phenomena such as surface-stress-driven nonlinear elastic stiffening or softening [66] of both the bulk and surface are not allowed to occur within this framework. In contrast, because the SCB model is based upon finite deformation kinematics, such effects are naturally captured.

3. Numerical examples

All numerical examples were performed on three-dimensional, $\langle 100\rangle$ single crystal silicon nanowires of length L, square cross section of width a, and unreconstructed {100} transverse surfaces. We considered nanowires of width a ranging from $a=12$ to $a=30$ nm, and with aspect ratios of $L/a=$ 8, 16, 24 and 32; the geometries are summarized in Table 2. All simulations were performed using the Sandia-developed simulation code Tahoe [67].

Table 2
Summary of nanowire geometries considered: constant aspect ratios of $L/a=8$ (CAR1), $L/a=16$ (CAR2), $L/a=24$ (CAR3), $L/a=32$ (CAR4). All dimensions are in nanometers (nm) in the form $L\times a\times a$.

CAR1	CAR2	CAR3	CAR4
$96\times 12\times 12$	$192\times 12\times 12$	$288\times 12\times 12$	$384\times 12\times 12$
$120\times 15\times 15$	$240\times 15\times 15$	$360\times 15\times 15$	$480\times 15\times 15$
$144\times 18\times 18$	$288\times 18\times 18$	$432\times 18\times 18$	$576\times 18\times 18$
$168\times 21\times 21$	$336\times 21\times 21$	$504\times 21\times 21$	$672\times 21\times 21$
$192\times 24\times 24$	$384\times 24\times 24$	$576\times 24\times 24$	$768\times 24\times 24$
$240\times 30\times 30$	$480\times 30\times 30$	$720\times 30\times 30$	$960\times 30\times 30$

Author's personal copy

Two different boundary conditions, fixed/fixed and fixed/free ends, were considered; these are similar to those previously utilized in experimental studies of nanowire bending [19,68,69]. All FE simulations were performed using regular meshes of 8-node hexahedral elements, where the number of elements ranged from 4096 to 256,000, while each element had a constant cube length of 1.5 nm. The T3 version of the Tersoff potential for silicon [51] was utilized to calculate the bulk and surface stresses for the SCB model; we note that for all geometries and boundary conditions both SCB and BCB bending simulations were carried out, to determine the effects of surface stresses on the elastic properties of silicon nanowires as compared to the corresponding bulk material, i.e. the BCB model which does not account for surface stress effects.

For both boundary conditions, the nanowires were first relaxed to their minimum energy configurations before any external loading was carried out; the nanowires are initially out of equilibrium due to the surface stresses, and at equilibrium the compressive surface stresses are balanced by tensile stresses that develop in the nanowire bulk. We note that the effects of the bulk tensile stresses are naturally captured by the nonlinear BCB model. Once the minimum energy (deformed) configuration due to surface stresses was determined, an external force was applied incrementally under quasistatic loading, such that the nanowire could equilibrate due to a given load increment before additional loading was applied. The elastic properties and the bending stresses were determined after applying bending strains of 8.5e−3%; this strain value is arbitrary and was simply chosen to be sufficiently small such that nonlinear elastic bending deformations would not be induced.

3.1. Nanowire elastic properties

The multiscale FE simulations of the bending of silicon nanowires using either the SCB or BCB models enables us to determine the bending stiffness k of the nanowires, which can be directly calculated from

$$\Delta F = k\Delta d, \tag{29}$$

where Δd is the increment in bending displacement that results from the increment in applied force ΔF, and k is the spring constant-like stiffness that relates the force and displacement.

The bending stiffness k is also a critical parameter because it enables experimentalists to, using the assumptions of linear elastic continuum beam theory, estimate the nanowire Young's modulus E using known solutions for fixed/fixed and fixed/free beams, where the stiffness $k = 192EI/L^3$ for a fixed/fixed beam loaded at the beam center, and $k = 3EI/L^3$ for a fixed/free beam loaded at the free end.

The results for the bulk-normalized bending stiffness for all geometries and both boundary conditions are summarized in Figs. 3 and 4. We first discuss results for the fixed/free nanowires in Fig. 3, where there are two trends of interest. First, we find that for all cross sectional sizes, the fixed/free nanowires are slightly stiffer elastically than the corresponding bulk material, with the stiffness increase being between 3 and 5% larger than the bulk material. This slight increase in effective stiffness occurs for fixed/free boundary conditions because the compressive silicon surface stresses [10] cause the nanowire to elongate axially. The fixed/free nanowires therefore exists at equilibrium in a tensile state of strain, which explains the slightly higher effective elastic properties as seen in Fig. 3 as compared to the bulk value. Second, we note that the stiffness increase decreases with increasing cross sectional size, which makes sense as larger nanowires should have elastic properties that approach the bulk value.

As shown in Fig. 4, the results for the fixed/fixed silicon nanowires are completely different. First, we notice that for smaller aspect ratios, i.e. $L/a=8$, all nanowires regardless of cross sectional size have a stiffness that is essentially bulk-like. However, once the aspect ratio is increased for a given nanowire cross sectional size, a significant decrease in elastic stiffness (as compared to the corresponding bulk material) is observed. For example, the Young's modulus for the $a=12$ nm cross section silicon nanowire with aspect ratio of 32 is nearly 50% smaller than the bulk Young's modulus. More significantly, this trend of a decreasing Young's modulus with increasing aspect ratio is observed even for the largest cross sectional sizes we have considered, i.e. for the $a=30$ nm cross section nanowire, the Young's modulus is almost 20% smaller than the bulk Young's modulus when the aspect ratio is increased to 32.

These results have significant implications for the comparisons that are made between computational (molecular dynamics) or theoretical results with experimental results for nanowire elastic properties. One reason is because the nanowires that are studied experimentally typically have extremely large aspect ratios; for example, in the recent work of Zhu et al. [26], the nanowires that

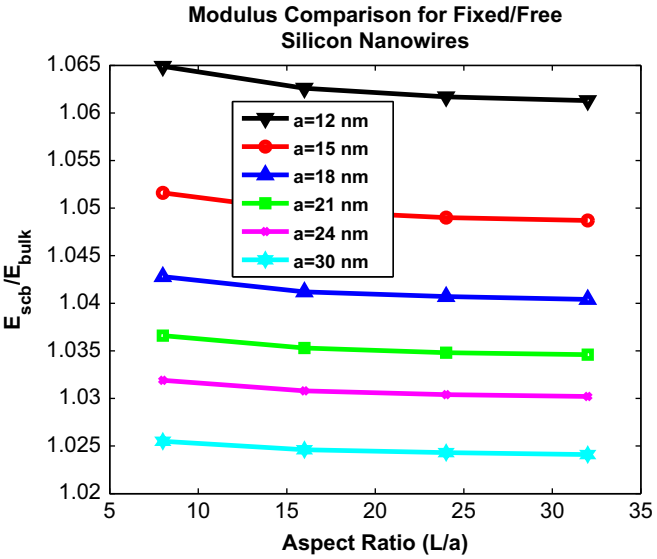

Fig. 3. Size-dependent Young's modulus of fixed/free silicon nanowires with various cross sectional sizes and aspect ratios.

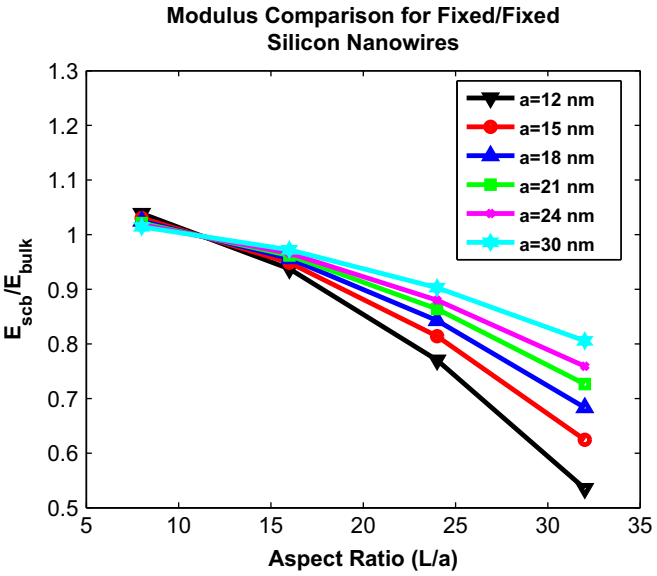

Fig. 4. Size-dependent Young's modulus of fixed/fixed silicon nanowires with various cross sectional sizes and aspect ratios.

Author's personal copy

were tensile loaded had aspect ratios ranging from 70 to 100. Similarly, silicon nanowires that were recently studied experimentally by Sadeghian et al. [22] and Zheng et al. [23] had aspect ratios exceeding 100.

In contrast, the aspect ratios of the silicon nanowires that have been studied computationally are relatively small, particularly in comparison to those that have been studied experimentally. For example, MD simulations of silicon nanowires by various authors [29,30,70] considered silicon nanowires with aspect ratios between 2 and 10. The significance of this finding is that the elastic softening we have observed in Fig. 4 does not manifest itself strongly until the nanowire aspect ratio exceeds about 15, which may explain why previous MD simulations have reported essentially bulk elastic properties for nanowires with cross sectional sizes larger than about 10 nm.

For DFT calculations, periodic boundary conditions are often considered in the axial direction to mimic an infinitely long nanowire. However, these axial direction boundary conditions neglect surface effects that occur on the two axial surfaces; furthermore, DFT calculations typically use hydrogen bonds to passivate the silicon transverse surfaces, which further mitigates any surface effects.

Because of the seeming importance of nanowire aspect ratio on the effective elastic properties, we discuss this effect further by comparing the obtained SCB results in Figs. 3 and 4 with a well-known surface elastic theory that forms the basis for many of such theories that have recently appeared in the literature [35].

3.2. Comparison to linear surface elastic model

We compare the SCB results in Figs. 3 and 4 to the analytic surface elastic solution derived by He and Lilley [35], which includes the effects of both surface stress and surface stiffness on the effective Young's modulus of nanowires; we also note the similarity of the He and Lilley model to concurrent work by Wang and Feng [71]. Specifically, the He and Lilley model is representative of many such theoretical surface elastic models because it utilizes the surface elastic relationship of Gurtin and Murdoch [53] for the surface constitutive model through the Young–Laplace equations.

To utilize the He and Lilley model to compare against the SCB results, numerical values for the surface stress and surface elastic constants (surface stiffness) are required. Therefore, we utilize the surface elastic constants derived from the Tersoff T3 potential, which formed the basis for both the BCB and SCB models we have utilized. These surface elastic constants for the T3 potential were recently evaluated by Izumi et al. [72], who reported the following values: $\tau^0 = -0.88$ N/m and $\mathbf{C}_0 = -8.07$ N/m for unreconstructed {100} surfaces of silicon.

The analytic solutions for fixed/fixed and fixed/free nanowires as derived by He and Lilley [35] can be written as

$$\left(\frac{E_{eff}}{E}\right)_{fixed/fixed} = \frac{H^0 L^2}{4Ea^4[1-\frac{4\tanh(\sqrt{\eta}/4)}{\sqrt{\eta}}]}, \tag{30}$$

and

$$\left(\frac{E_{eff}}{E}\right)_{fixed/free} = \frac{4H^0 L^2}{Ea^4\cosh(\sqrt{\eta})[1-\frac{\tanh(\sqrt{\eta})}{\sqrt{\eta}}]}, \tag{31}$$

where $H^0 = 2a\tau_0$, a is the square cross sectional length of the nanowire, $\eta = H^0 L^2/(EI)^*$ is the nondimensional surface effect factor and $(EI)^*$ is the effective bending modulus which is defined as

$$(EI)^* = EI_1 + \frac{1}{2}\mathbf{C}_0 a^3 + \frac{1}{6}\mathbf{C}_0 a^3, \tag{32}$$

where $I_1 = a^4/12$ is the moment of inertia of the square cross section.

We note that (30)–(32) suggest that the surface effects will impact the elastic properties in a different manner depending upon the boundary condition that is used to fix the nanowires. This hypothesis was confirmed by both the analytic results of He and Lilley [35], as well as by Park et al. using multiscale resonance calculations [44,46].

We compare the results of the analytic models and the SCB calculations for the fixed/fixed nanowires in Fig. 5. The trends observed between the SCB results and the analytic solution are similar. First, both show, for a cross sectional size, a decrease in effective Young's modulus with increasing nanowire length, or increasing aspect ratio. Second, the agreement between the He and Lilley predictions and the SCB predictions improve with an increase in the nanowire cross sectional dimensions.

The similarities between the SCB and the analytic model with regard to their strong aspect ratio and size-dependence arise from the fact that the He and Lilley model has an effective dependence on L^2/a^3, or the square of the aspect ratio divided by the nanowire cross sectional length. Therefore, while the actual magnitudes of the size and aspect ratio-dependence of the analytic model as compared to the SCB results vary depending on the other scaling factors that multiply or add to the L^2/a^3 term, both solutions show the same trends, at least for the fixed/fixed case.

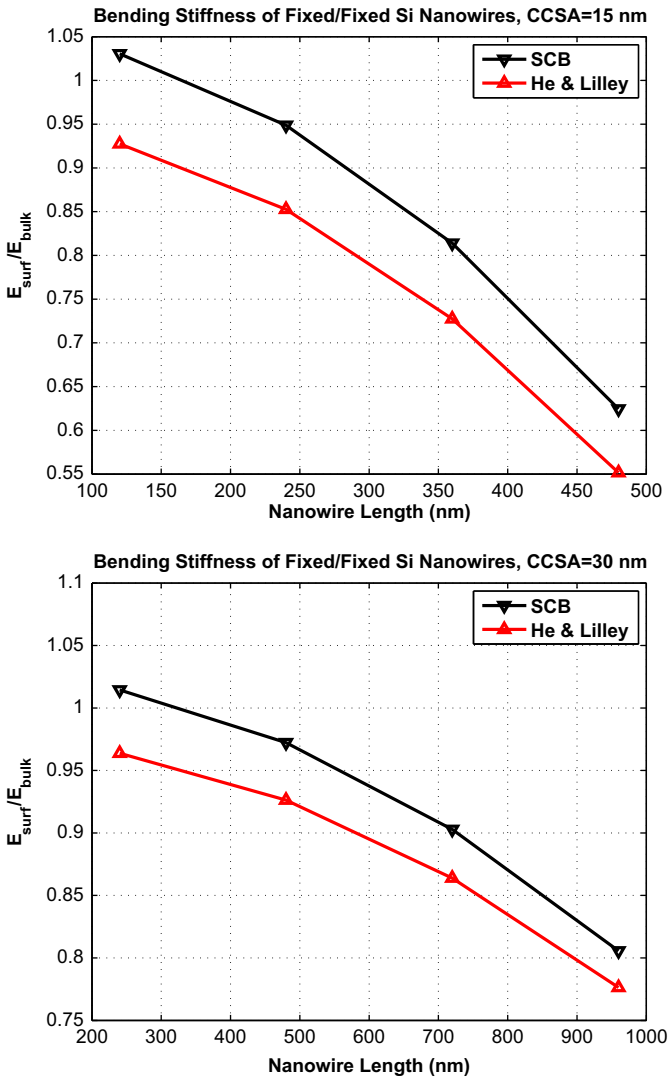

Fig. 5. Size-dependent Young's modulus of fixed/fixed silicon nanowires as compared using SCB and He and Lilley [35] solutions for 15 and 30 nm cross section nanowires of various length.

Author's personal copy

While the SCB results are generally similar to the analytic solution for the fixed/fixed boundary conditions, a much different story is found for the fixed/free boundary conditions. As seen in Fig. 6 for the fixed/free silicon nanowires with a constant cross sectional lengths of 15 and 30 nm, the SCB predicts an essentially size-independent, or constant effective Young's modulus with decreasing cross sectional size. However, the analytic solution shows greatly divergent results.

Specifically, the He and Lilley solution predicts a significant increase in effective Young's modulus with increasing nanowire length, or aspect ratio. While (30) and (31) show that the He and Lilley model does predict a boundary condition dependence in the effective elastic properties, the predicted stiffness increase of nearly a factor of 14 for the 15 nm cross sectional silicon nanowire has not been observed in any experimental or computational results to-date. For the nanowires with a 30 nm cross sectional length, the He and Lilley solution still predicts a significant stiffening with increasing nanowire length, though the predicted increase is only a factor of 2.5 when the aspect ratio increases to 32 (length=960 nm).

The fact that the analytic surface elastic solution shows reduced accuracy, or seemingly unphysical results for the fixed/free boundary conditions can be explained as follows. As discussed earlier for fixed/free boundary conditions, the SCB model allows the nanowire to elongate axially in order to alleviate the compressive silicon surface stresses. The nanowire therefore exists in a slightly tensile state of strain, which explains the slightly higher effective elastic properties as seen in Fig. 3 as compared to the bulk value.

In contrast, the He and Lilley analytic model does not account for surface-stress-driven axial elongation. The major issue then is that the He and Lilley model does not account for residual stresses in the *bulk* of the nanowire that must develop in response to the surface-stress-driven axial elongation of the fixed/free nanowires. Furthermore, changes in the surface stress and surface elastic properties that occur due to deformation that is induced by surface stresses are not accounted for due to the constant nature of the surface properties. Despite this, the He and Lilley model predicts an elastic stiffening for the fixed/free boundary condition, albeit significantly higher than is predicted by the SCB model. These results collectively indicate that while the surface elastic models are useful in bringing physical insights to understanding how surface effects impact the elastic properties of nanowires, they are not always accurate for all boundary conditions, a finding that was previously made by Yun and Park [48].

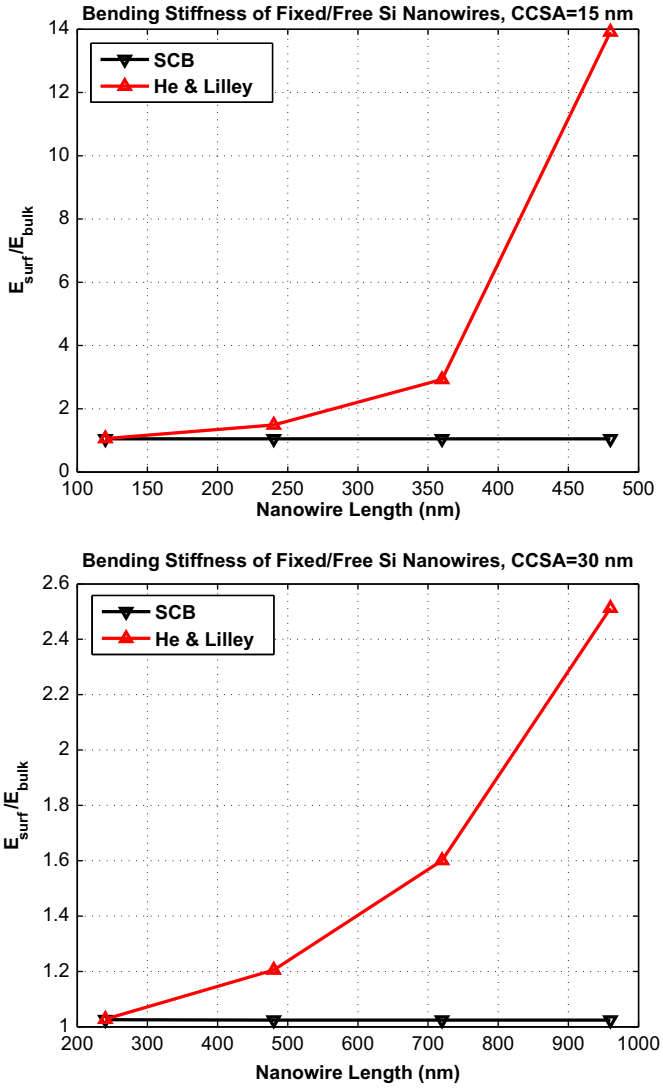

Fig. 6. Size-dependent Young's modulus of fixed/free silicon nanowires as compared using SCB and He and Lilley [35] solutions for 15 and 30 nm cross section nanowires of various length.

4. Conclusions

In conclusion, we have utilized the recently developed multiscale, finite element-based surface Cauchy–Born model to bring insights into the reasons underlying the disparity between the elastic properties reported theoretically and experimentally for silicon nanowires. Specifically, we have found that there is a substantial difference in the aspect ratios of nanowires that have been considered experimentally, where the nanowire aspect ratios often exceed about 100, as compared to those that have been considered theoretically or computationally, where the nanowire aspect ratios are typically smaller than 10.

By using the surface Cauchy–Born model to study silicon nanowires with cross sectional sizes between 12 and 30 nm, with aspect ratios between 8 and 32 for each geometry, we have found that significant elastic softening is observed, which is in line with previous experimental studies. The significance of this finding is that the elastic softening we have observed does not manifest itself strongly until the nanowire aspect ratio exceeds about 15, which may explain why previous MD simulations have reported essentially bulk elastic properties for nanowires with cross sectional sizes larger than about 10 nm.

By using the multiscale surface Cauchy–Born model, we have also found significant elastic softening for silicon nanowires with 30 nm cross sectional sizes, which is far larger than the bulk elastic properties that are reported using atomistic simulations for short aspect ratio nanowires with cross sectional sizes smaller than 10 nm. The strong aspect ratio dependence is also predicted by existing analytic models, although the models can predict unreasonably high or low effective Young's modulus for certain boundary conditions.

Acknowledgments

HSP gratefully acknowledges NSF grant number CMMI-0750395 in support of this research. GY gratefully acknowledges the support of the Mechanical Engineering department at the University of Colorado. Both authors acknowledge helpful discussions with Prof. Carmen M. Lilley.

Author's personal copy

References

[1] Y. Xia, P. Yang, Y. Sun, Y. Wu, B. Mayers, B. Gates, Y. Yin, F. Kim, H. Yan, One-dimensional nanostructures: synthesis, characterization, and applications, Adv. Mater. 15 (2003) 353–389.

[2] C.M. Lieber, Z.L. Wang, Functional nanowires, MRS Bull. 32 (2007) 99–108.

[3] K. Eom, H.S. Park, D.S. Yoon, T. Kwon, Nanomechanical resonators and their applications in biological/chemical detection: nanomechanics principles, Phys. Rep. 503 (2011) 115–163.

[4] L.T. Canham, Silicon quantum wire array fabricated by electrochemical and chemical dissolution of wafers, Appl. Phys. Lett. 57 (1990) 1046–1048.

[5] R. He, P. Yang, Giant piezoresistive effect in silicon nanowires, Nat. Nanotechnol. 1 (2006) 42–46.

[6] A.I. Boukai, Y. Bunimovich, J. Tahir-Kheli, J.-K. Yu, W.A. Goddard, J.R. Heath, Silicon nanowires as efficient thermoelectric materials, Nature 451 (2008) 168–171.

[7] A.I. Hochbaum, R. Chen, R.D. Delgado, W. Liang, E.C. Garnett, M. Najarian, A. Majumdar, P. Yang, Enhanced thermoelectric performance of rough silicon nanowires, Nature 451 (2008) 163–168.

[8] D. Li, Y. Wu, P. Kim, L. Shi, P. Yang, A. Majumdar, Thermal conductivity of individual silicon nanowires, Appl. Phys. Lett. 83 (2003) 2934–2936.

[9] H.S. Park, W. Cai, H.D. Espinosa, H. Huang, Mechanics of crystalline nanowires, MRS Bull. 34 (2009) 178–183.

[10] H. Balamane, T. Halicioglu, W.A. Tiller, Comparative study of silicon empirical interatomic potentials, Phys. Rev. B 46 (1992) 2250–2279.

[11] H.W. Shim, L.G. Zhou, H. Huang, T.S. Cale, Nanoplate elasticity under surface reconstruction, Appl. Phys. Lett. 86 (2005) 151912.

[12] C.Q. Sun, B.K. Tay, X.T. Zeng, S. Li, T.P. Chen, J. Zhou, H.L. Bai, E.Y. Jiang, Bond-order-bond-length-bond-strength (bond-OLS) correlation mechanism for the shape-and-size dependence of a nanosolid, J. Phys.: Condens. Matter 14 (2002) 7781–7795.

[13] J. Diao, K. Gall, M.L. Dunn, Surface-stress-induced phase transformation in metal nanowires, Nat. Mater. 2 (2003) 656–660.

[14] W. Liang, M. Zhou, F. Ke, Shape memory effect in Cu nanowires, Nano Lett. 5 (2005) 2039–2043.

[15] H.S. Park, K. Gall, J.A. Zimmerman, Shape memory and pseudoelasticity in metal nanowires, Phys. Rev. Lett. 95 (2005) 255504.

[16] H.S. Park, C. Ji, On the thermomechanical deformation of silver shape memory nanowires, Acta Mater. 54 (2006) 2645–2654.

[17] X. Li, T. Ono, Y. Wang, M. Esashi, Ultrathin single-crystalline-silicon cantilever resonators: fabrication technology and significant specimen size effect on Young's modulus, Appl. Phys. Lett. 83 (2003) 3081–3083.

[18] A. Heidelberg, L.T. Ngo, B. Wu, M.A. Phillips, S. Sharma, T.I. Kamins, J.E. Sader, J.J. Boland, A generalized description of the elastic properties of nanowires, Nano Lett. 6 (2006) 1101–1106.

[19] A.S. Paulo, J. Bokor, R.T. Howe, R. He, P. Yang, D. Gao, C. Carraro, R. Maboudian, Mechanical elasticity of single and double clamped silicon nanobeams fabricated by the vapor-liquid-solid method, Appl. Phys. Lett. 87 (2005) 053111.

[20] M. Tabib-Azar, M. Nassirou, R. Wang, S. Sharma, T.I. Kamins, M.S. Islam, R.S. Williams, Mechanical properties of self-welded silicon nanobridges, Appl. Phys. Lett. 87 (2005) 113102.

[21] S. Hoffmann, I. Utke, B. Moser, J. Michler, S.H. Christiansen, V. Schmidt, S. Senz, P. Werner, U. Gosele, C. Ballif, Measurement of the bending strength of vapor-liquid-solid grown silicon nanowires, Nano Lett. 6 (2006) 622–625.

[22] H. Sadeghian, C.K. Yang, J.F.L. Goosen, E. van der Drift, A. Bossche, P.J. French, F. van Keulen, Characterizing size-dependent effective elastic modulus of silicon nanocantilevers using electrostatic pull-in instability, Appl. Phys. Lett. 94 (2009) 221903.

[23] K. Zheng, X. Han, L. Wang, Y. Zhang, Y. Yue, Y. Qin, X. Zhang, Z. Zhang, Atomic mechanisms governing the elastic limit and incipient plasticity of bending si nanowires, Nano Lett. 9 (2009) 2471–2476.

[24] T. Kizuka, Y. Takatani, K. Asaka, R. Yoshizaki, Measurements of the atomistic mechanics of single crystalline silicon wires of nanometer width, Phys. Rev. B 72 (2005) 035333.

[25] X. Han, K. Zheng, Y.F. Zhang, X. Zhang, Z. Zhang, Z.L. Wang, Low-temperature in situ large-strain plasticity of silicon nanowires, Adv. Mater. 19 (2007) 2112–2118.

[26] Y. Zhu, F. Xu, Q. Qin, W.Y. Fung, W. Lu, Mechanical properties of vapor-liquid-solid synthesized silicon nanowires, Nano Lett. 9 (2009) 3934–3939.

[27] J.Q. Broughton, C.A. Meli, P. Vashishta, R.K. Kalia, Direct atomistic simulation of quartz crystal oscillators: bulk properties and nanoscale devices, Phys. Rev. B 56 (1997) 611–618.

[28] B. Lee, R.E. Rudd, First-principles calculation of mechanical properties of Si 〈001〉 nanowires and comparison to nanomechanical theory, Phys. Rev. B 75 (2007) 195328.

[29] K. Kang, W. Cai, Brittle and ductile fracture of semiconductor nanowires - molecular dynamics simulations, Philos. Mag. 87 (2007) 2169–2189.

[30] M. Menon, D. Srivastava, I. Ponomareva, L.A. Chernozatonskii, Nanomechanics of silicon nanowires, Phys. Rev. B 70 (2004) 125313.

[31] P.W. Leu, A. Svizhenko, K. Cho, Ab initio calculations of the mechanical and electronic properties of strained si nanowires, Phys. Rev. B 77 (2008) 235305.

[32] H.S. Park, P.A. Klein, G.J. Wagner, A surface Cauchy–Born model for nanoscale materials, Int. J. Numer. Methods Eng. 68 (2006) 1072–1095.

[33] H.S. Park, P.A. Klein, Surface Cauchy–Born analysis of surface stress effects on metallic nanowires, Phys. Rev. B 75 (2007) 085408.

[34] H.S. Park, P.A. Klein, A surface Cauchy–Born model for silicon nanostructures, Comput. Methods Appl. Mech. Eng. 197 (2008) 3249–3260.

[35] J. He, C.M. Lilley, Surface effect on the elastic behavior of static bending nanowires, Nano Lett. 8 (2008) 1798–1802.

[36] E. Tadmor, M. Ortiz, R. Phillips, Quasicontinuum analysis of defects in solids, Philos. Mag. A 73 (1996) 1529–1563.

[37] E.B. Tadmor, G.S. Smith, N. Bernstein, E. Kaxiras, Mixed finite element and atomistic formulation for complex crystals, Phys. Rev. B 59 (1999) 235–245.

[38] Z. Tang, H. Zhao, G. Li, N.R. Aluru, Finite-temperature quasicontinuum method for multiscale analysis of silicon nanostructures, Phys. Rev. B 74 (2006) 064110.

[39] H. Zhao, Z. Tang, G. Li, N.R. Aluru, Quasiharmonic models for the calculation of thermodynamic properties of crystalline silicon under strain, J. Appl. Phys. 99 (2006) 064314.

[40] P. Zhang, Y. Huang, P.H. Geubelle, P.A. Klein, K.C. Hwang, The elastic modulus of single-wall carbon nanotubes: a continuum analysis incorporating interatomic potentials, Int. J. Solids Struct. 39 (2002) 3893–3906.

[41] M. Arroyo, T. Belytschko, An atomistic-based finite deformation membrane for single layer crystalline films, J. Mech. Phys. Solids 50 (2002) 1941–1977.

[42] G. Yun, H.S. Park, A finite element formulation for nanoscale resonant mass sensing using the surface Cauchy–Born model, Comput. Methods Appl. Mech. Eng. 197 (2008) 3324–3336.

[43] G. Yun, H.S. Park, A multiscale, finite deformation formulation for surface stress effects on the coupled thermomechanical behavior of nanomaterials, Comput. Methods Appl. Mech. Eng. 197 (2008) 3337–3350.

[44] H.S. Park, P.A. Klein, Surface stress effects on the resonant properties of metal nanowires: the importance of finite deformation kinematics and the impact of the residual surface stress, J. Mech. Phys. Solids 56 (2008) 3144–3166.

[45] H.S. Park, Surface stress effects on the resonant properties of silicon nanowires, J. Appl. Phys. 103 (2008) 123504.

[46] H.S. Park, Quantifying the size-dependent effect of the residual surface stress on the resonant frequencies of silicon nanowires if finite deformation kinematics are considered, Nanotechnology 20 (2009) 115701.

[47] H.S. Park, Strain sensing through the resonant properties of deformed metal nanowires, J. Appl. Phys. 104 (2008) 013516.

[48] G. Yun, H.S. Park, Surface stress effects on the bending properties of fcc metal nanowires, Phys. Rev. B 79 (2009) 195421.

[49] H.S. Park, A multiscale finite element method for the dynamic analysis of surface-dominated nanomaterials, Int. J. Numer. Methods Eng. 83 (2010) 1237–1254.

[50] H.S. Park, M. Devel, Z. Wang, A new multiscale formulation for the electromechanical behavior of nanomaterials, Comput. Methods Appl. Mech. Eng. 200 (2011) 2447–2457.

[51] J. Tersoff, Modeling solid-state chemistry: interatomic potentials for multicomponent systems, Phys. Rev. B 39 (1989) 5566–5568.

[52] J. Tersoff, New empirical approach for the structure and energy of covalent systems, Phys. Rev. B 37 (1988) 6991–7000.

[53] M.E. Gurtin, A. Murdoch, A continuum theory of elastic material surfaces, Arch. Ration. Mech. Anal. 57 (1975) 291–323.

[54] T. Belytschko, W.K. Liu, B. Moran, Nonlinear Finite Elements for Continua and Structures, John Wiley and Sons, 2002.

[55] T.J.R. Hughes, The Finite Element Method: Linear Static and Dynamic Finite Element Analysis, Prentice-Hall, 1987.

[56] J. Yvonnet, H.L. Quang, Q.-C. He, An XFEM/level set approach to modelling surface/interface effects and to computing the size-dependent effective properties of nanocomposites, Comput. Mech. 42 (2008) 119–131.

[57] W. Gao, S. Yu, G. Huang, Finite element characterization of the size-dependent mechanical behaviour in nanosystems, Nanotechnology 17 (2006) 1118–1122.

[58] J. He, C.M. Lilley, The finite element absolute nodal coordinate formulation incorporated with surface stress effect to model elastic bending nanowires in large deformation, Comput. Mech. 44 (2009) 395–403.

[59] H. She, B. Wang, A geometrically nonlinear finite element model of nanomaterials with consideration of surface effects, Finite Elem. Anal. Des. 45 (2009) 463–467.

[60] M. Farsad, F.J. Vernerey, H.S. Park, An extended finite element/level set method to study surface effects on the mechanical behavior and properties of nanomaterials, Int. J. Numer. Methods Eng. 84 (2010) 1466–1489.

[61] R.C. Cammarata, Surface and interface stress effects in thin films, Prog. Surf. Sci. 46 (1994) 1–38.

[62] V.B. Shenoy, Atomistic calculations of elastic properties of metallic FCC crystal surfaces, Phys. Rev. B 71 (2005) 094104.

[63] J. Wang, Z. Huang, H. Duan, S. Yu, X. Feng, G. Wang, W. Zhang, T. Wang, Surface stress effect in mechanics of nanostructured materials, Acta Mech. Solida Sin. 24 (2011) 52–82.

[64] A. Javili, P. Steinmann, A finite element framework for continua with boundary energies. part I: the two-dimensional case, Comput. Methods Appl. Mech. Eng. 198 (2009) 2198–2208.

[65] A. Javili, P. Steinmann, A finite element framework for continua with boundary energies. part II: the three-dimensional case, Comput. Methods Appl. Mech. Eng. 199 (2010) 755–765.

[66] H. Liang, M. Upmanyu, H. Huang, Size-dependent elasticity of nanowires: nonlinear effects, Phys. Rev. B 71 (2005) 241403 (R).

[67] Tahoe, 〈http://sourceforge.net/projects/tahoe/〉 (2011).

Author's personal copy

[68] S. Cuenot, C. Frétigny, S. Demoustier-Champagne, B. Nysten, Surface tension effect on the mechanical properties of nanomaterials measured by atomic force microscopy, Phys. Rev. B 69 (2004) 165410.
[69] G.Y. Jing, H.L. Duan, X.M. Sun, Z.S. Zhang, J. Xu, Y.D. Li, J.X. Wang, D.P. Yu, Surface effects on elastic properties of silver nanowires: contact atomic-force microscopy, Phys. Rev. B 73 (2006) 235409.
[70] Y. Jing, Q. Meng, Y. Gao, Molecular dynamics simulation on the buckling behavior of silicon nanowires under uniaxial compression, Comput. Mater. Sci. 45 (2009) 321–326.
[71] G.-F. Wang, X.-Q. Feng, Surface effects on the buckling of nanowires under uniaxial compression, Appl. Phys. Lett. 94 (2009) 141913.
[72] S. Izumi, S. Hara, T. Kumagai, S. Sakai, A method for calculating surface stress and surface elastic constants by molecular dynamics: application to the surface of crystal and amorphous silicon, Thin Solid Films 467 (2004) 253–360.